Weierstraß–Institut
für Angewandte Analysis und Stochastik

im Forschungsverbund Berlin e.V.

Preprint ISSN 0946 – 8633

Simulation of Static and Dynamic Properties of Edge-Emitting Multi Quantum Well Lasers

U. Bandelow, R. Hünlich, T. Koprucki

submitted: December 12th 2002

Weierstrass Institute for
Applied Analysis and Stochastics
Mohrenstraße 39
D – 10117 Berlin, Germany
E-Mail:
bandelow@wias-berlin.de
huenlich@wias-berlin.de
koprucki@wias-berlin.de

Preprint No. 799

Berlin 2002

2000 *Mathematics Subject Classification*. 78A60, 68U20.

Key words and phrases. Semiconductor lasers, quantum wells, device simulation, multi section lasers.

1999 *PACS Numbers*. 42.55.Px, 73.20.Dx, 85.60.Bt, 78.66.Fd.

Edited by
Weierstraß–Institut für Angewandte Analysis und Stochastik (WIAS)
Mohrenstraße 39
D — 10117 Berlin
Germany

Fax: + 49 30 2044975
E-Mail: preprint@wias-berlin.de
World Wide Web: http://www.wias-berlin.de/

Simulation of Static and Dynamic Properties of Edge-Emitting Multi Quantum Well Lasers

U. Bandelow, R. Hünlich, T. Koprucki

Abstract

This paper demonstrates simulation tools for edge-emitting multi quantum well (MQW) lasers. Properties of the strained MQW active region are simulated by eight-band kp calculations. Then, a 2D simulation along the transverse cross section of the device is performed based on a drift-diffusion model, which is self-consistently coupled to heat transport and equations for the optical field. Furthermore, a method is described, which allows for an efficient quasi 3D simulation of dynamic properties of multi-section edge-emitting lasers.

I. Introduction

Coverage of effects on many scales, ranging from semiconductor nanostructures to macroscopic optical resonators, is required in the quantitative analysis of devices. For the modeling of semiconductor lasers a hierarchy of models representing the different scales can be derived. This paper demonstrates corresponding simulation tools for long-wavelength edge-emitting MQW lasers.

The response of a strained MQW structure to external excitation is very sensitive to the electronic band structure and to the transition matrix elements. The calculation of these quantities for the active region of strained MQW lasers will be subject of section II. These data can then be used as input for more comprehensive device simulations. The model and results from example calculations obtained with our 2D device simulator WIAS-TeSCA will be presented in section III. Within WIAS-TeSCA, the carrier- and energy transport is described by drift-diffusion equations coupled to a heat transport equation [1]. The distribution of the optical field is described by Helmholtz equations, the evolution of its intensity is due to a photon balance equation. The latter gives a simplistic picture of the longitudinal structure of the device.

To extend the applicability to multi-section edge-emitting lasers this paper presents in section IV a model which allows for the calculation of their stationary as well as dynamic properties in a quasi 3D setting. The idea bases on the TPP-method[1] published earlier in [2], which allowed for the calculation of combined longitudinal and transverse spatial hole burning effects in multi-section laser diodes in the stationary case. Basically, the TPP-method provided a sophisticated data management which allowed for a considerable reduction of computational effort for (quasi-) 3D problems. Here, the TPP-method is firstly extended to the non-stationary case with multi-longitudinal mode dynamics. A substantially simplified version of the quasi 3D model can be obtained in the single mode case, which applies to most of the present applications.

II. MQW Data

We have computed the optical response function as well as other properties of the strained MQW active region of III-V semiconductor lasers by kp calculations with WIAS-QW [3]. Thereby, the quantum confined states $F_{\mu l}(y;\mathbf{k}_{\|})$ and the corresponding sub-band dispersions $E_l(\mathbf{k}_{\|})$ are solutions of the respective

The authors are with WIAS Berlin

[1]**T**reat **P**ower as a **P**arameter

eigenvalue problem

$$H_{\mu\nu}\left(\mathbf{k}_{\|}, k_{\perp}=-i\frac{\partial}{\partial y};\ldots\right)F_{\nu l}(y;\mathbf{k}_{\|})=E_l(\mathbf{k}_{\|})F_{\mu l}(y;\mathbf{k}_{\|}) \tag{1}$$

where y denotes the growth direction. For consistently modeling the mixing of conduction- and valence bands we use eight-band kp Hamiltonians $H_{\mu\nu}$. The structure of these Hamiltonians can be found in more detail in [4], their spectral properties have been studied in [5]. The band mixing causes non-parabolic dispersion for the valence- and conduction sub-bands as well and predicts consistently the interband transition matrix elements. Throughout the remainder of this section we will illustrate this by an example. Our example is a $\mathrm{Ga}_x\mathrm{In}_{1-x}\mathrm{As}_y\mathrm{P}_{1-y}$ strained MQW structure which is designed for emission at 1.55μm, see Fig. 6. The structure consists of six 1% compressively strained 7 nm thick quantum wells ($x=0.239, y=0.826$), which are separated by 10 nm thick 0.3% tensile strained barriers ($x=0.291, y=0.539$).

A. Band-structure Calculations

Typically, as in our example, the barrier width in the active region of a MQW laser is designed for a decoupling of the wells, which forces the lowest states to be localized in the individual quantum wells. We firstly have controlled this feature by the corresponding mini-band formation, which is illustrated in Fig. 1. No dispersion is observed for the lowest conduction- and highest valence mini-bands, which most contribute to the interband transitions. For this reason we have confined to single quantum well calculations for the remaining investigations in this section.

The sub-band dispersion $E_l(\mathbf{k}_{\|})$ for our example quantum well is drawn in Fig. 2. Due to the compressive strain in the well the light hole (LH)–heavy hole (HH) degeneracy at $\mathbf{k}=0$ is lifted such that the uppermost two valence sub-bands correspond to HH-like states. The dispersion is shown for two different crystallographic directions in the $\mathbf{k}_{\|}$-plane, which displays the warping (angular dependence) effect. Fig. 2 shows weak warping for conduction sub-bands, but strong warping for the valence sub-bands.

In addition, from the solutions $F_{\nu i}=F_{\nu i}(y;\mathbf{k}_{\|})$ of (1) we have calculated the intersubband momentum matrix elements $\mathbf{p}_{ij}=\mathbf{p}_{ij}(\mathbf{k}_{\|})$ according to [4]:

$$\mathbf{p}_{ij}=\frac{m_0}{\hbar}\sum_{\mu,\nu}\left\langle F_{\mu i}\middle|\nabla_{\mathbf{k}}H_{\mu\nu}\left(\mathbf{k}_{\|},k_{\perp};\ldots\right)\Big|_{ik_{\perp}=\frac{\partial}{\partial y}}\middle|F_{\nu j}\right\rangle, \tag{2}$$

($m_0=$ free electron mass) which in particular enter the optical transition rates as in (11) and in (12). The squared moduli of the most important interband momentum matrix elements are depicted in Fig. 3 for different polarization directions $\mathbf{e}$. We observe strong dispersion of these matrix elements and warping especially for the main transition $\mathrm{CB}_1 \leftrightarrow \mathrm{HH}_1$ for TE-polarization. The main transition almost exclusively contributes to the TE-polarization which is therefore favoured by our particular structure. This feature is at least in consequence to the compressive strain in the wells, which energetically favours the heavy holes, as shown in Fig. 1 and Fig. 2.

B. Density of States and Material Gain

If the Fermi levels E_{Fn} and E_{Fp} of the quantum confined carriers are given, then their sheet concentrations N and P are obtained by

$$N = \sum_{i\in c}\int\frac{d^2\mathbf{k}_{\|}}{(2\pi)^2}f\Big(E_i(\mathbf{k}_{\|})-E_{Fn}\Big) \tag{3}$$

$$P = \sum_{j\in v}\int\frac{d^2\mathbf{k}_{\|}}{(2\pi)^2}f\Big(E_{Fp}-E_j(\mathbf{k}_{\|})\Big) \tag{4}$$

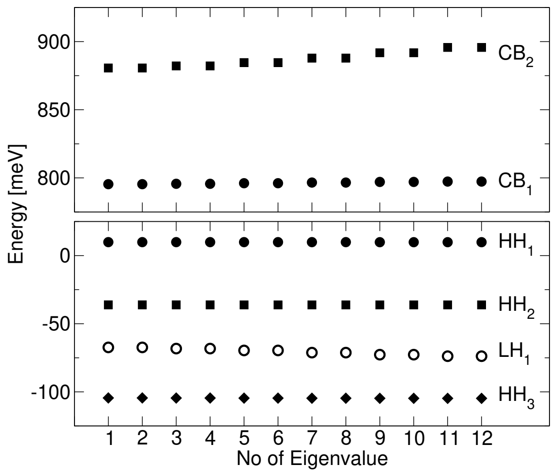

Fig. 1. Mini-band formation in our example MQW structure consisting of 6 quantum wells. Due to symmetry all eigenvalues are twice degenerate, yielding groups of 12 eigenvalues. Top: conduction band states, bottom: valence band states, both for $\mathbf{k}_{\|} = 0$. The lowest conduction- and highest valence mini-bands exhibit no dispersion, whereas the higher mini-bands do, indicating an increasing coupling between the states in the individual wells.

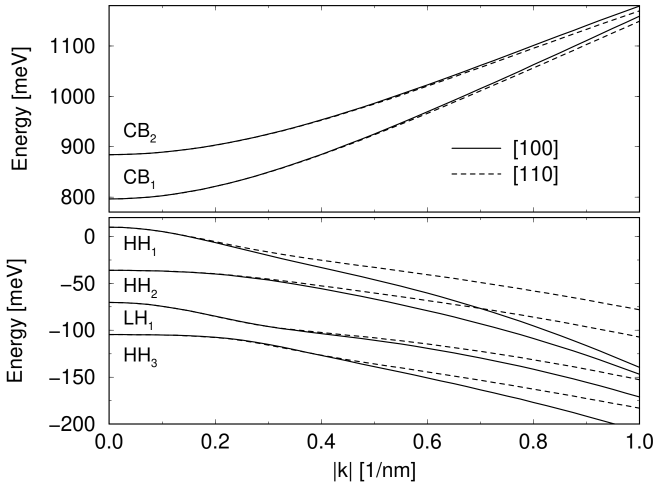

Fig. 2. Sub-band dispersion and warping in a 7nm InGaAsP compressively strained quantum well, calculated with WIAS-QW. Top: conduction sub-bands, bottom: valence sub-bands. $\mathbf{k}_{\|}$ in [100]- (solid) and [110]-direction (dashed). We remark that the sub-bands are twice degenerate due to symmetry.

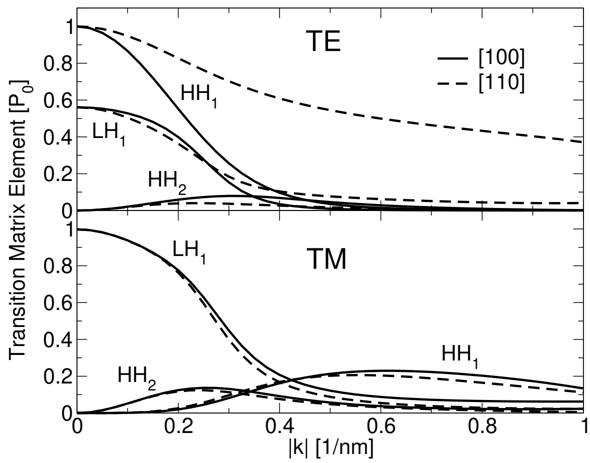

Fig. 3. Momentum matrix element dispersion $|\mathbf{e}\mathbf{p}_{ij}(\mathbf{k}_{\|})|^2$ (2) for transitions between the lowest conduction sub-band CB_1 shown in Fig. 2 top, and the upper valence sub-bands shown in Fig 2 bottom. Different polarization directions $\mathbf{e}$ are shown. Top: TE-polarization $(\mathbf{p}||\mathbf{e}_x)$, bottom: TM-polarization $(\mathbf{p}||\mathbf{e}_y)$. Note the normalization to the same quantity P_0 in both pictures.

with the Fermi distribution

$$f(E) = \left(1 + \exp\left(\frac{E}{k_B T}\right)\right)^{-1}, \tag{5}$$

where k_B denotes the Boltzmann constant and T the temperature. Due to the nearly complete localization of the carriers in the quantum well we can introduce *average* carrier densities per quantum well $n = N/d_{qw}$ and $p = P/d_{qw}$, where d_{qw} is the thickness of the well. By this definition we obtain from our eight-band kp calculations the relations

$$n = n\left(E_{Fn}, k_B T\right), \quad p = p\left(E_{Fp}, k_B T\right) \tag{6}$$

for the averaged carrier densities, which are plotted in Fig. 4 and Fig. 5, respectively. Both functions can be reasonably fitted to the Fermi-Dirac distributions

$$n = N_c \mathcal{F}_{1/2}\left(\frac{E_{Fn} - E_c}{k_B T}\right) \tag{7}$$

$$p = N_v \mathcal{F}_{1/2}\left(\frac{E_v - E_{Fp}}{k_B T}\right). \tag{8}$$

used in the drift-diffusion model by adjusting the effective band-edges E_c and E_v and the corresponding band-edge densities of state N_c and N_v. The latter have been adjusted by masses m_α according to the generic relation

$$N_\alpha = 2\left(\frac{m_\alpha k_B T}{2\pi\hbar^2}\right)^{3/2}. \tag{9}$$

$\mathcal{F}_{1/2}$ in (7), (8) is the Fermi-integral of order $1/2$:

$$\mathcal{F}_{1/2}(x) = \frac{2}{\sqrt{\pi}}\int_0^\infty \frac{\sqrt{y}}{1+\exp(y-x)}dy. \tag{10}$$

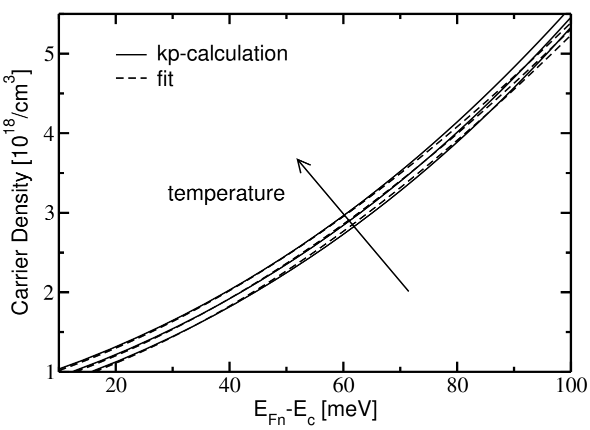

Fig. 4. Relation (6) (kp-calculation) between electron density n and Fermi level E_{Fn} relative to the net band edge E_c for temperatures T=290K, 315K, 340K. The dashed lines indicate the fit to the macroscopic state-equation (7).

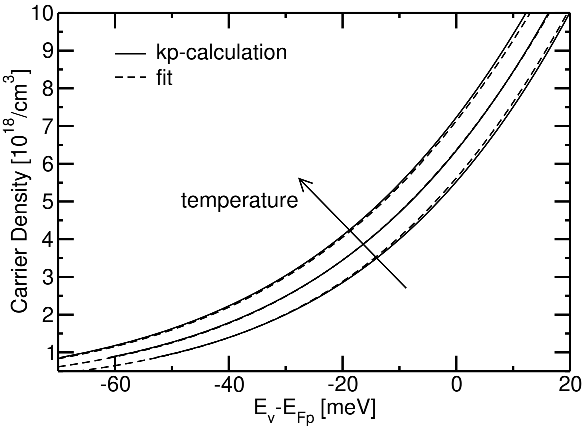

Fig. 5. Relation (6) (kp-calculation) between hole density p and Fermi level E_{Fp} relative to the net band edge E_v for temperatures T=290K, 315K, 340K. The dashed lines indicate the fit to the macroscopic state-equation (8).

The fit for the valence bands is very close to the calculated curve for a wide range of densities and temperatures, see Fig. 5, whereas for the conduction bands the Fermi-Dirac distribution (7) yields a good approximation for a more restricted range of parameters, see Fig. 4. This enables us to effectively treat individual quantum wells as specific classical materials with microscopic defined band-edges and band-edge densities of state. Note that the offsets $\Delta E_c = E_c - E_{c0}$ and $\Delta E_v = E_v - E_{v0}$ between the adjusted 'macroscopic' band-edges E_c and E_v and the band-edges E_{c0} and E_{v0} of the calculated bandstructure (see Fig. 2) are -4.2 meV and -15.5 meV, respectively, leading to a slightly larger 'macroscopic' bandgap.

Using the momentum matrix elements (2) we have calculated the material gain according to

$$\begin{aligned} g(\omega) &= \frac{\pi\hbar q^2}{\varepsilon_0 m_0^2 n_r c}\frac{1}{d_{qw}}\sum_{\substack{i\in c\\ j\in v}}\int\frac{d^2\mathbf{k}_\parallel}{(2\pi)^2}\frac{|\mathbf{p}_{ij}\mathbf{e}|^2}{E_i-E_j}f(E_i-E_{Fn})\left(1-f(E_j-E_{Fp})\right)\times \\ &\quad \left[1-\exp\left(\frac{\hbar\omega-(E_{Fn}-E_{Fp})}{k_BT}\right)\right]\frac{1}{\pi}\frac{\Gamma}{[(E_i-E_j)-\hbar\omega]^2+\Gamma^2}, \end{aligned} \tag{11}$$

where the last factor includes broadening due to collision processes [6]. The latter have been parametrized by a characteristic intra-band relaxation time τ of 60 fs ($\Gamma = \hbar/\tau$). q denotes the elementary charge, c the speed of light and n_r the refractive index. Assuming an undoped active region we have used local charge neutrality $n = p$ for all calculations in the following. Calculated gain spectra are drawn in Fig. 6 for different excitations and temperatures. There was almost no difference between MQW-calculations and our corresponding single QW results, which strongly supports our conclusions drawn from Fig. 1. The evolution of the corresponding maximum material gain with the carrier density is drawn in Fig. 7 for different temperatures. For sufficiently high densities (above $2.5\cdot 10^{18}$ cm^{-3}) the maximum material gain

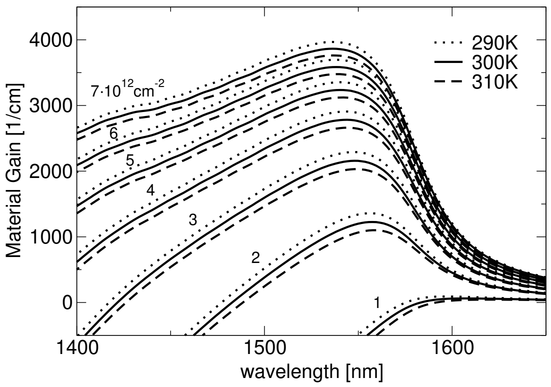

Fig. 6. Material gain spectra (TE-polarization) according to (11) for different sheet concentrations and temperatures.

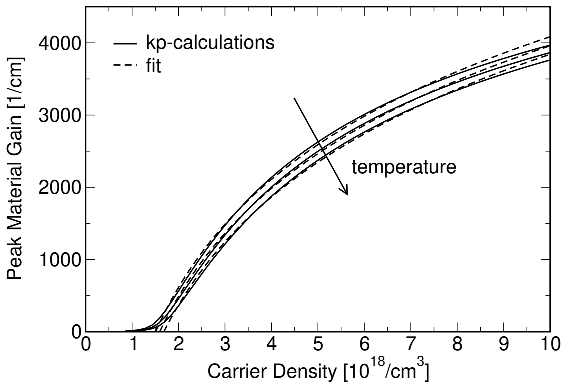

Fig. 7. Maximum material gain for different carrier densities and temperatures T=290K, 300K, 310K. Dashed lines indicate the fit to the logarithmic gain model $g(n) = g_0 \log(n/n_t)$. Whereas $g_0 = 2155\text{cm}^{-1}$ is not very sensitive to the temperature and has been kept constant here, the transparency density $n_t = n_t(T)$ roughly linearly increases with the temperature.

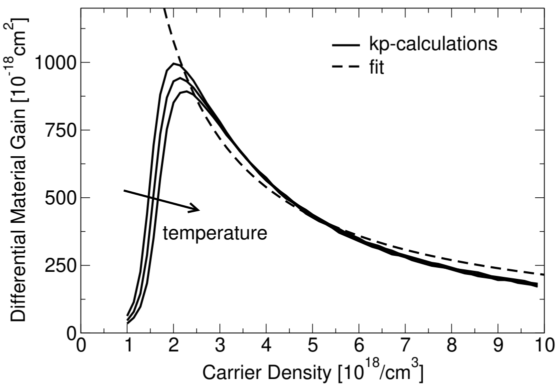

Fig. 8. Differential gain, taken at the spectral maximum of the material gain in Fig. 6 for different carrier densities and temperatures. The fit corresponds to Fig. 7, i.e. $dg/dn = g_0/n$, which is independent on the temperature.

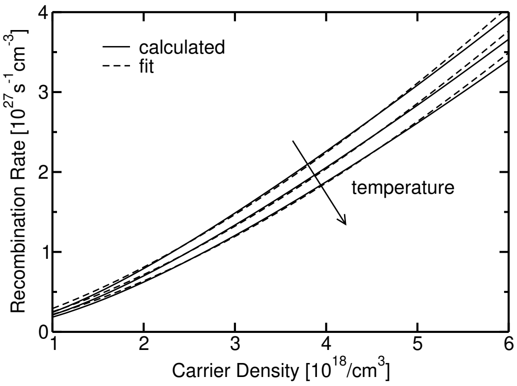

Fig. 9. Spontaneous radiative recombination rate (12) for different temperatures T=290K, 315K, 340K. Dashed: fit to $R_{rad} = B \cdot n^{\alpha}$, with $\alpha = 1.47$ $(290K)$, 1.51 $(315K)$, 1.55 $(340K)$.

may be well fitted by a logarithmic model $g(n) = g_0 \log(n/n_t)$, see Fig. 7. However, for low densities the fit completely fails. Whereas g_0 is not very sensitive to the temperature and has been kept constant here, the transparency density n_t should roughly linearly increase with the temperature. This can be clearly seen by the differential gain, which is depicted in Fig. 8. The fit drawn in Fig. 8 is according to Fig. 7, hence $dg/dn = g_0/n$ with the same g_0, which is independent on the temperature. Exclusively the range of validity for the logarithmic fit slightly shifts with the temperature.

Furthermore, using the momentum matrix elements (2) again we have calculated the spontaneous radiative recombination rate R_{rad} according to [7]

$$R_{rad} = \frac{n_r q^2}{\pi \hbar^2 c^3 \varepsilon_0 m_0^2} \frac{1}{d_{qw}} \frac{1}{4\pi^2} \sum_{\substack{i \in c \\ j \in v}} \int d^2\mathbf{k}_{\|} \, (E_i - E_j) \left|\mathbf{p}_{ij}\right|^2 f(E_i - E_{Fn}) f(E_{Fp} - E_j) \qquad (12)$$

which significantly influences the threshold current if the active region is undoped ($n = p$). The spontaneous radiative recombination rate is shown in Fig. 9 together with the fit to $R_{rad} = B \cdot n^{\alpha}$. The exponent was approximately $\alpha = 1.5$ which differs from the commonly used models corresponding to $\alpha = 2$.

III. Device Simulation

Our example device is a 400 μm long single-section InP-based strained multi-quantum well Fabry-Perot type ridge-waveguide (RW) laser, the transverse cross-section of which is depicted in part in Fig. 10, with a ridge width of 2.4μm.
The device simulation has been performed by means of the code WIAS-TeSCA [8]. Within WIAS-TeSCA, the carrier transport is described by the drift-diffusion equations

$$\begin{aligned} \varepsilon_0 \nabla_\perp (\varepsilon_s \nabla_\perp \varphi) &= -q(C + p - n), && (13) \\ q\frac{\partial n}{\partial t} - \nabla_\perp \cdot \mathbf{j}_n &= -qR - q\frac{v_g}{L} g(\omega)|\Xi|^2 S, && (14) \\ q\frac{\partial p}{\partial t} + \nabla_\perp \cdot \mathbf{j}_p &= -qR - q\frac{v_g}{L} g(\omega)|\Xi|^2 S && (15) \end{aligned}$$

for the electrostatic potential φ and the carrier distributions n, p in the transverse cross section of the laser. In (13) ε_s is the static dielectric constant and C is the net doping profile. $\nabla_\perp = (\partial_x, \partial_y, 0)^T$ is the transverse part of the Nabla operator. Recently, the drift-diffusion model (13)-(15) has been coupled to a heat transport equation [1]. Within the resulting energy model the currents are driven by the gradients of the quasi-Fermi potentials F_n and F_p, respectively, and by the gradient of the temperature T. The quasi-Fermi potentials are linked with the carrier concentrations by means of Fermi-Dirac statistics:

$$\begin{aligned} n &= N_c \mathcal{F}_{1/2}\left(\frac{q\varphi - qF_n - E_c}{k_B T}\right), && (16) \\ p &= N_v \mathcal{F}_{1/2}\left(\frac{E_v + qF_p - q\varphi}{k_B T}\right), && (17) \end{aligned}$$

where E_c denotes the conduction and E_v the valence band edge. The recombination rate R in (14), (15) involves all non-radiative and radiative spontaneous recombination processes. The recombination processes stimulated by the optical field are involved by the last terms in (14), (15), where v_g denotes the group velocity and L the length of the laser, Ξ and S will be discussed in the next subsection.

A. Optics

Assuming stable transverse waveguiding allows us to express the main component of the optical field vector $E(\mathbf{r}, t)$

$$E(\mathbf{r}, t) = e^{i\omega t} \left[\Psi^+(z,t)e^{-ikz} + \Psi^-(z,t)e^{ikz}\right] \Xi_0(\mathbf{r}_\perp) \qquad (18)$$

in terms of the transverse main mode $\Xi_0(\mathbf{r}_\perp)$. Transverse modes $\Xi(\mathbf{r}_\perp)$ are eigensolutions of the waveguide equation

$$\left[\nabla_\perp^2 + \frac{\omega^2}{c^2}\varepsilon_{opt}(\omega, \mathbf{r}_\perp) - \beta^2\right] \Xi(\mathbf{r}_\perp) = 0, \qquad (19)$$

corresponding to their respective (complex) eigenvalues β.[2]
$\varepsilon_{opt}(\omega, \mathbf{r}_\perp) = (n_r(\omega, \mathbf{r}_\perp) + ic\left[g(\omega, \mathbf{r}_\perp) - \alpha_{bg}(\mathbf{r}_\perp)\right]/2\omega)^2$ denotes the complex dielectric function of the pumped laser averaged over one section in longitudinal direction. Via the gain $g(\omega, \mathbf{r}_\perp)$ (11), the background absorption $\alpha_{bg}(\mathbf{r}_\perp)$ and the refractive index $n_r(\omega, \mathbf{r}_\perp)$ the dielectric function ε_{opt} depends on almost all properties of the device and its operating state, as well as on properties of the optical field, as its polarization and its frequency.

In 2D-simulations with WIAS-TeSCA, longitudinal properties are only considered by assuming a longitudinally homogeneous power distribution, which is approximately met in Fabry-Perot lasers or in edge-emitting lasers with properly designed Bragg gratings [2]. In our calculations the fundamental mode

[2] Eq. (19) is formulated here for TE-polarization. TM polarization can be counted for as well, without restrictions for the considerations here, but with a different version of (19).

shown in Fig. 10 has been involved, the number of photons S of which is balanced by a corresponding photon rate equation

$$\dot{S} = v_g(2\Im m\beta - \alpha)S + R^{spont}, \tag{20}$$

where R^{spont} is short for the spontaneous emission into the mode, α is the sum of longitudinal scattering- and output losses at the facets and the modal gain $\Im m\beta$ is the imaginary part of the corresponding eigenvalue subject to (19). The photon rate equation (20) is valid for Fabry-Perot resonators with a constant shaped longitudinal field distribution.

With the above model we have calculated static properties of our example device first. As shown in Fig. 11, the threshold current is 12 mA and the range below 100 mA exhibits a linear power-current characteristic. This indicates neglectable influence of heating in this region of operation, where also stable single mode emission is detected. At higher currents heating effects appear, which decrease the quantum efficiency of the device. This can be seen by the curved power-current characteristic above 150 mA in Fig. 11. For the analysis of the modulation response, which will be the subject of the next subsection, we will concentrate on the non-thermal region of operation, which is indicated in particular by the circles in Fig. 11.

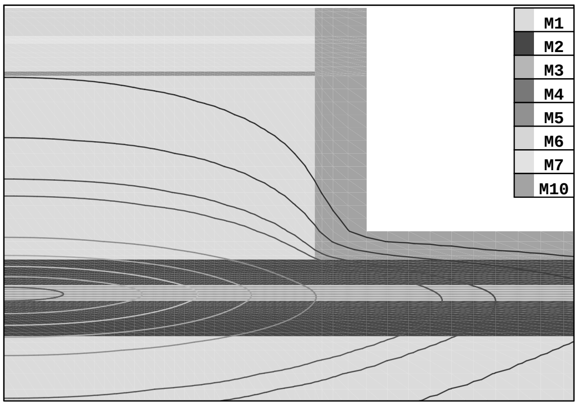

Fig. 10. Intensity distribution of the fundamental transverse TE-mode in a cross section of our RW laser, calculated with WIAS-TeSCA. Due to symmetry only the right half plane has been considered, which only partially is shown. The different Materials M_i are indicated by different shading.

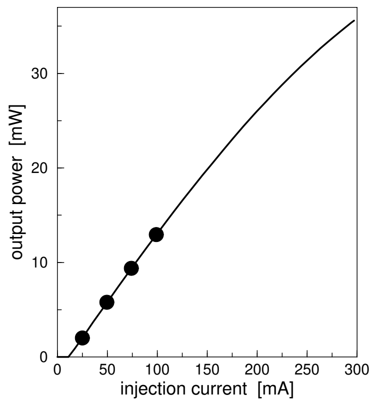

Fig. 11. Power-current characteristic of the RW laser shown in Fig. 10. Below 100 mA the characteristic is linear, at higher currents heating effects come into play. The filled circles indicate the operation points, for which the modulation response has been calculated.

B. Modulation Response

The photon balance equation (20) self-consistently closes the drift-diffusion model (13)-(20). In particular, this allows us to study the small-signal modulation response of the device, as drawn in Fig. 12 and Fig. 13. Moreover, the large-signal behaviour of the device can be studied in the time domain, as illustrated by the pulse response in Fig. 14. Although being accessible within WIAS-TeSCA, we have dropped influences from effects as nonlinear gain saturation [9] for all the examples presented here, to keeping them simple.

The modulation response drawn in Fig. 12 has been obtained with WIAS-TeSCA by a small-signal analysis. We found out, that the (normalized) response function $H_n(\omega) = H(\omega)/H(0)$ can be very well fitted by

$$H_n(\omega) = e^{-i\omega\theta} \frac{1}{1 + i\omega\tau} \frac{\omega_r^2}{\omega_r^2 - \omega^2 + i\Gamma_r\omega} \tag{21}$$

as demonstrated in Fig. 13. The last factor in (21) is well known from rate equation models [9]. The response is modified by the first two factors in (21) which are a time delay and a low pass filter, respectively. These modifications must be caused by higher-order effects due to the drift-diffusion transport through the two-dimensional cross section of the device, including the strained MQW active region.

Moreover, we can alternatively use the large-signal capabilities of WIAS-TeSCA for studying the response of the device due to a pulse excitation in the time domain. The power response $\Delta P(t)$ is drawn in Fig. 14 and can be almost perfectly fitted by

$$\Delta P(t) = c_1 e^{-t/\tau} + c_2 \cos(\sqrt{\omega_r^2 - \Gamma_r^2/4}t + \delta) e^{-\Gamma_r t/2}, \tag{22}$$

where c_1, c_2 and δ also have to be adjusted as functions of ω_r, Γ_r, τ and θ. The parameters extracted in this manner coincide well with the values obtained by the small-signal analysis.

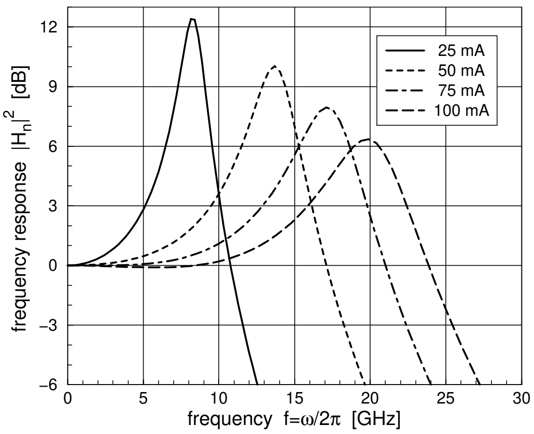

Fig. 12. Modulation response $|H_n(\omega)|^2$ (21) of the RW laser, as in Fig. 10, obtained by small-signal analysis.

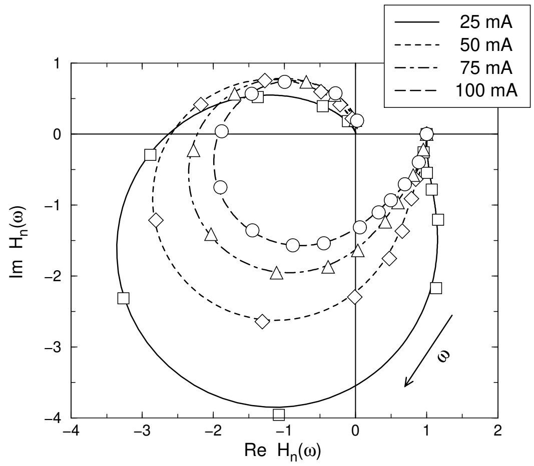

Fig. 13. Complex response functions $H_n(\omega)$. The symbols are results obtained by small-signal analysis while the lines are computed with (21) using extracted parameters as plotted in Fig. 15.

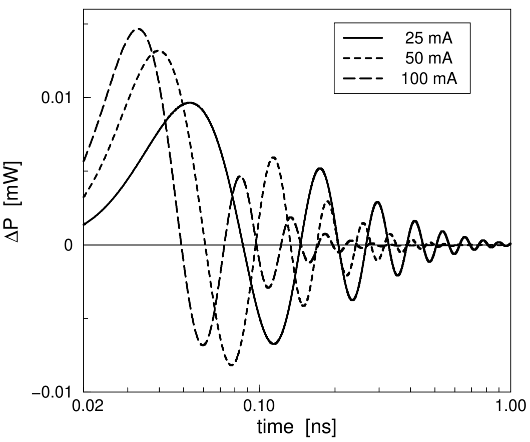

Fig. 14. Pulse response of the RW laser for 3 different bias points.

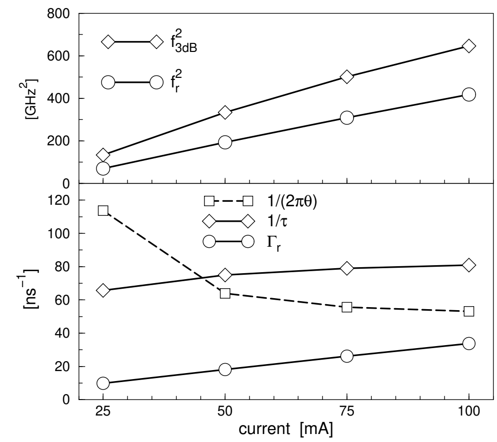

Fig. 15. Extracted characteristic frequencies (top), damping parameters and delay time θ (bottom) for the modulation response.

Fig. 15 shows the frequency $f_r = \omega_r/2\pi$ and the 3dB frequency f_{3dB} corresponding to the response level 1/2. The linear dependence of the squared frequency f_r on the injection current is in complete agreement to the rate equation model [9]. Also, the linear dependence of the damping parameter Γ_r on the injection current, as shown in Fig. 15, agrees with the suggestions from the rate equation model. In conclusion, the modulation response of the device may be surprisingly well fitted to the standard rate equation result, but modified by a phenomenological low pass filter and a time delay.

IV. QUASI 3D COUPLING

So far, the considerations above have been restricted to simplistic single-section longitudinal structures. To overcome this restriction we propose in this section a quasi 3D coupling model for multi-section lasers which resolves the 2D transport equations (13)–(19) in each transverse cross-section s, coupled to each other by the equations for the longitudinal evolution of the optical field:

$$-\frac{i}{v_g}\frac{\partial}{\partial t}\Psi^+ = \left(i\frac{\partial}{\partial z} - \beta + k + i\frac{\alpha_0}{2}\right)\Psi^+ - \kappa^+\Psi^- \tag{23}$$

$$-\frac{i}{v_g}\frac{\partial}{\partial t}\Psi^- = \left(-i\frac{\partial}{\partial z} - \beta + k + i\frac{\alpha_0}{2}\right)\Psi^- - \kappa^-\Psi^+. \tag{24}$$

The function β in (23), (24) is stepwise constant on each section s and given by the fundamental eigenvalue β_s of the transverse waveguide equation (19) for the cross section s. In (23), (24) α_0 are the longitudinal propagation losses and $\kappa^\pm$ is the coupling coefficient due to the presence of gratings as in DFB-lasers, which can vary along the laser axis. Spontaneous emission, usually included by additional stochastic terms $f_{sp}^\pm$ in (23), (24) has been omitted here for simplicity. The traveling wave equations (TWE) (23), (24) are accomplished by the boundary conditions at the end facets of the laser

$$\Psi^+(z=0,t) = r_0\Psi^-(z=0,t), \tag{25}$$

$$\Psi^-(z=L,t) = r_L\Psi^+(z=L,t). \tag{26}$$

From the solution of (23), (24) the number of photons S_s

$$S_s(t) = \frac{1}{L_s}\int_{L_s}\left(\left|\Psi^+(z,t)\right|^2 + \left|\Psi^-(z,t)\right|^2\right)dz \tag{27}$$

in each section s with length L_s can be obtained. These enter the transport equations (13)–(19) by the stimulated recombination term in (14), (15). This generic coupling of the transverse to the longitudinal model via the optical power was the observation which led to the TPP method [2] derived earlier for the stationary case. The coupling proposed here, which is illustrated in Fig. 16, leads to a transient model for the 3D evolution of the optical field. Rather than a direct numerical simulation of the whole device, each transverse cross-section can be discretized independently and solved in parallel. The TWE have their own discretization along z and act as the master equation in this scheme, sketched in Fig. 16.

In many applications the devices are designed for stable single mode emission. In this case we can use the correct single mode photon rate equation [10]

$$\frac{d}{dt}S = -2\Im m[\Omega]S + \frac{1}{2}\left(\frac{d}{dt}K\right)S + R^{spont}, \tag{28}$$

for the number of photons S in the main mode, instead of the partial differential equations (23), (24) for the field amplitudes. To see this, we note the following form of the TWE (23), (24), c.f. [11]:

$$-i\frac{\partial}{\partial t}\Psi = H(z)\Psi \tag{29}$$

where $H(z)$ is a linear operator [12]. Simplification can be achieved now by expressing $\Psi(z,t) = \left(\Psi^+(z,t),\Psi^-(z,t)\right)^T$ in terms of instantaneous modes $\Phi_l(z) = \left(\Phi^+(z),\Phi^-(z)\right)_l^T$, which are eigensolutions to $H(z)$:[3]

$$H(z)\Phi_l(z) = \Omega_l\Phi_l(z) \tag{30}$$

subject to the boundary conditions (25), (26). Reflecting the lossy nature of the laser cavity, $H(z)$ has a complex eigenvalue spectrum $\{\Omega_l\}$. The real parts $\Re e[\Omega_l]$ refer to the frequencies of the cavity modes and the imaginary parts $\Im m[\Omega_l]$ refer to their damping in time. Stationary states, as we seek for, are

[3] More precise, $\Psi(z,t)$ has to be expanded in the set of root functions of $H(z)$, as proven in [13]. The set of root functions includes the eigenfunctions obtained from (30) as well as Jordan chains in cases of degeneracy. The latter don't apply for stationary cases, but are usually connected with complicated dynamic scenarios [11].

realized if the lasing mode $\Phi_0(z)$ is undamped (i.e. $\Im m[\Omega_0] = 0$) and all other modes are damped (i.e. $\Im m[\Omega_l] > 0$ for all l except $l = 0$). This means that all modes except the lasing mode can be dropped. Consequently, the field amplitude in a stationary state is

$$\Psi(z,t) = e^{i\Omega_0 t}\Phi_0(z) \tag{31}$$

with a real lasing frequency Ω_0. Compared to the TWE-model this is a powerful and exact expression for stationary states, requiring only the solution of the eigenvalue problem (30) instead of solving the partial differential equations (23), (24) in space and time.

Moreover, one can use the single mode approximation (28) for calculating dynamic properties of multi-section lasers, as stability, bifurcation scenarios or the modulation response, because Eq. (28) applies also to multi-section lasers under single mode conditions. This has been demonstrated in [10], where the importance of the dynamic losses $\left(\frac{d}{dt}K\right)$ has been studied. The appearance of the longitudinal Petermann K-factor

$$K = \left| \frac{\int(|\Phi_l^+(z)|^2 + |\Phi_l^-(z)|^2)dz}{2\int \Phi_l^+(z)\Phi_l^-(z)dz} \right|^2 \tag{32}$$

is in consequence to the lossy nature of the resonator, and its time derivative counts for a changing field distribution.[4] Moreover, the appearance of such Petermann factors in dynamic equations for the mode amplitudes in lossy resonators has been shown to be very general in [14]. For single section Fabry-Perot resonators with a constant shaped longitudinal field distribution the dynamic losses $\frac{d}{dt}K$ disappear and the photon balance equation (28) becomes identical to Eq. (20).

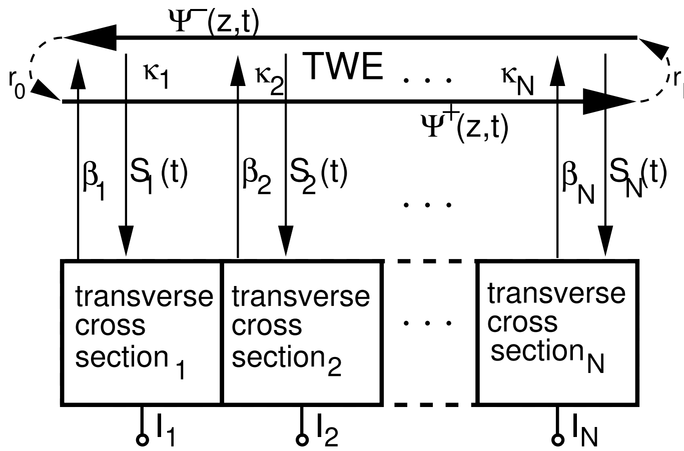

Fig. 16. Scheme for the coupling of models for the transverse cross sections s (boxes) which can be driven by individual injection currents I_s to the longitudinal TWE model for a multi-section edge-emitting laser. The coupling of each cross section s to the TWE is realized via the corresponding photon number S_s (27) and the fundamental eigenvalue β_s from (19).

V. Conclusion

We have demonstrated simulation tools for edge-emitting MQW lasers which cover the scales of size quantization and the carrier- and energy transport. In particular, properties of the strained MQW active region have been simulated by eight-band kp calculations. Then, we have demonstrated capabilities of our device simulator by more comprehensive simulations along the transverse cross section of a device. The latter simulation has been performed based on a drift-diffusion model, which is self-consistently coupled to heat transport and equations for the optical field. In this stage all quantities in the device simulator are self-consistently coupled and allow for the simulation of static and dynamic properties of single-section edge-emitting lasers. To extend the hierarchy of the models to multi-section edge-emitting lasers we have coupled the transverse transport- and waveguide equations (13)-(19) to the equations for the longitudinal evolution of the optical field amplitudes. This is promising for a quasi 3D simulation of stationary and transient properties of multi-section lasers. Under single mode conditions this model can be simplified by means of the photon rate equation (28).

[4]In the hermitian case (closed resonator, without losses or gain) K is equal to 1 and the second term disappears from (28).

Acknowledgment

The work of T. Koprucki has been supported by the Deutsche Forschungsgemeinschaft (SPP 1095), Grant No. FU 316/5-1. The authors thank H. Wenzel from FBH Berlin for the valuable discussions on laser modeling.

References

[1] G. Albinus, H. Gajewski, and R. Hünlich. Thermodynamic design of energy models of semiconductor devices. *Nonlinearity*, 15:367–383, 2002.

[2] H. J. Wünsche, U. Bandelow, and H. Wenzel. Calculation of combined lateral and longitudinal spatial hole burning in $\lambda/4$ shifted DFB lasers. *IEEE Journal of Quantum Electronics*, 29(6):1751–1761, 1993.

[3] U. Bandelow, H.-Chr. Kaiser, T. Koprucki, and J. Rehberg. Modeling and simulation of strained quantum wells in semiconductor lasers. In *Mathematische Verfahren zur Lösung von Problemstellungen in Industrie und Wirtschaft*. Springer-Verlag, to appear. (Preprint 582, WIAS, Berlin, 2000).

[4] P. Enders, A. Bärwolff, M. Woerner, and D. Suisky. kp theory of energy bands, wave functions, and optical selection rules in strained tetrahedral semiconductors. *Physical Review B*, 51(23):16695–16704, 1995.

[5] U. Bandelow, H.-Chr. Kaiser, T. Koprucki, and J. Rehberg. Spectral properties of $k \cdot p$ Schrödinger operators in one space dimension. *Numerical Functional Analysis and Optimization*, 21(3&4):379–409, 2000.

[6] P.M. Enders. Enhancement and spectral shift of optical gain in semiconductors from non–markovian intraband relaxation. *IEEE Journal of Quantum Electronics*, 33(4):580–588, 1997.

[7] Hans Wenzel. *How to use the kp8 programs*. [Online] Available: http://www.fbh-berlin.de/people/wenzel/kp8.html.

[8] H. Gajewski et al. *WIAS-TeSCA Two– and three–dimensional SemiConductor Analysis package*. Weierstrass Institute for Applied Analysis and Stochastics, Mohrenstraße 39, 10117 Berlin, Germany.

[9] S. L. Chuang. *Physics of optoelectronic Devices*. Wiley & Sons, New York, 1995.

[10] U. Bandelow, R. Schatz, and H.-J. Wünsche. A Correct Single Mode Photon Rate Equation for Multi-Section Lasers. *IEEE Phot. Techn. Lett.*, 8(5):614–617, 1996.

[11] H. Wenzel, U. Bandelow, H. J. Wünsche, and J. Rehberg. Mechanisms of Selfpulsations in 2-Section DFB-Lasers. *IEEE Journal of Quantum Electronics*, 32(1):69–79, 1996.

[12] U. Bandelow, M. Radziunas, J. Sieber, and M. Wolfrum. Impact of gain dispersion on the spatio-temporal dynamics of multisection lasers. *IEEE Journal of Quantum Electronics*, 37(2):183–188, 2001.

[13] J. Rehberg, H.-J. Wünsche, U. Bandelow, and H. Wenzel. Spectral Properties of a System describing fast pulsating DFB-Lasers. *ZAMM*, 77(1):75-77, 1997.

[14] H. Wenzel and H.-J. Wünsche. An Equation for the Amplitudes of the Modes in Semiconductor Lasers. *IEEE Journal of Quantum Electronics*, 30(9):2073–2080, 1994.